Aggregate Structures of Asymmetric Di-Alkyl Phosphate Anions and the Role of Conformations about the Polar Region: SANS, Cryo-TEM, Raman Scattering, ^{13}C NMR, and Selective NOE Studies

Sonoko Sasuga,[†] Daphne Weihs,[∥] Yeshayahu Talmon,*[‡] Hiro-Fumi Okabayashi,*[†] and Charmian J. O'Connor[§]
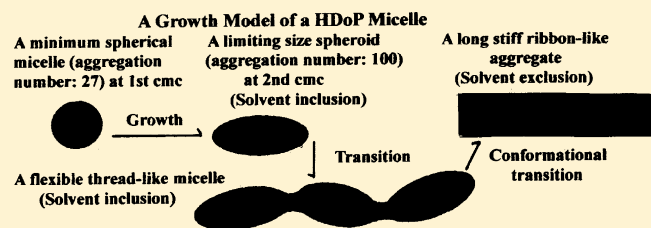
[†]Department of Applied Chemistry, Nagoya Institute of Technology, Gokiso-cho, Showa-ku, Aichi 466-8555, Japan
[‡]Faculty of Chemical Engineering, Technion-Israel Institute of Technology, Haifa 32000, Israel
[∥]Faculty of Biomedical Engineering, Technion-Israel Institute of Technology, Haifa 32000, Israel
[§]Department of Chemistry, The University of Auckland, Private Bag 92019, Auckland 1142, New Zealand

ABSTRACT: The aggregate structures of two di-n-alkyl-phosphate anions (di-n-alkyl: n-butyl(n-dodecyl)(BDoP) and n-hexyl(n-dodecyl)(HDoP)) in water were studied by the use of SANS, cryo-TEM, Raman scattering, ^{13}C NMR, and selective NOE (^{1}H{^{1}H}) techniques. The results of SANS indicated that the different $-CH_2-$ lengths of the short chain led to a marked difference in the aggregational behavior of BDoP and HDoP. Cryo-TEM added direct images to support the average aggregation size and shape predicted by the SANS analyses. Raman scattering, ^{13}C NMR, and selective NOE results provided further evidence that variation of molecular conformations strongly contributed to variation in the shape of the aggregates. In particular, selective NOE was a powerful technique for investigating the dynamic structures of the hydrocarbon chains during growth of the micelles.

A Growth Model of a HDoP Micelle

A minimum spherical micelle (aggregation number: 27) at 1st cmc

Growth

A limiting size spheroid (aggregation number: 100) at 2nd cmc (Solvent inclusion)

A long stiff ribbon-like aggregate (Solvent exclusion)

Transition

Conformational transition

A flexible thread-like micelle (Solvent inclusion)

INTRODUCTION

The type and microstructure of aggregates formed by surfactants depend on their geometrical packing properties,[1] which may be expected to vary readily with conformational change of the surfactant molecules.[2a−c,3−7] To discuss this problem in detail, systematic studies on the molecular design and synthesis of a surfactant and its aggregate structure are essential. In particular, the conformational change of a surfactant molecule upon aggregation becomes very relevant.

Raman scattering studies of simple surfactants have demonstrated that, out of all the possible rotational isomers about the CH_2-CH_2 single bond, one specific isomer is stabilized upon aggregation.[3−6] Results show that the conformational change of surfactant molecules always includes a disorder−order transition; a combination of inter- or intra-molecular hydrophobic interactions is the only driving force for such a conformational transition. This conformational change should be a major contributor to the variation in shape of an aggregate since such a transition alters the packing capability.

For an aggregated di-n-alkylphosphate (DAP) anion, conformational change about the two P−O bonds should contribute to the directionality of the two n-alkyl chains responsible for enhancement of hydrophobic interactions upon aggregation.[2a,5] For symmetric DAP, three molecular forms (GG, GT, and TT) and, for asymmetric DAP, four conformers (GG, GT, TG, and TT) are possible (Scheme 1).

Thermodynamic quantities for dimethylphosphate (DMP) have been calculated by Jayaram et al.[8] The calculation has

suggested that the intramolecular free energies favor the GG form relative to the GT and TT forms and that the energy differences are within $3k_BT$. These results may be applied to DAP with longer hydrocarbon chains.

Vibrational studies of DMP[9] have suggested that the GG form was stabilized in water. Conversely, depolarized Raleigh scattering and vibrational spectra of DMP[10] have indicated that the GT and TT forms are also highly populated.

Jayaram et al.[8] calculated the relative conformational free energies of hydration of DMP, using the hydration shell model proposed by Scheraga et al.[11] The results suggested that torsional angles of the phosphodiesters are in the GG form rather than the GT and TT forms and that the conformational differences between the free energies of hydration are small. These small free energy differences may be applied to DAP with longer hydrocarbon chains and support their preference for the other molecular forms.

The conformations of dibutyl and dipentyl phosphate anions have been studied by Raman scattering spectroscopy.[5,12] Depending on the water content, a specific rotational isomer about the P−O bonds was found to be stabilized preferentially.
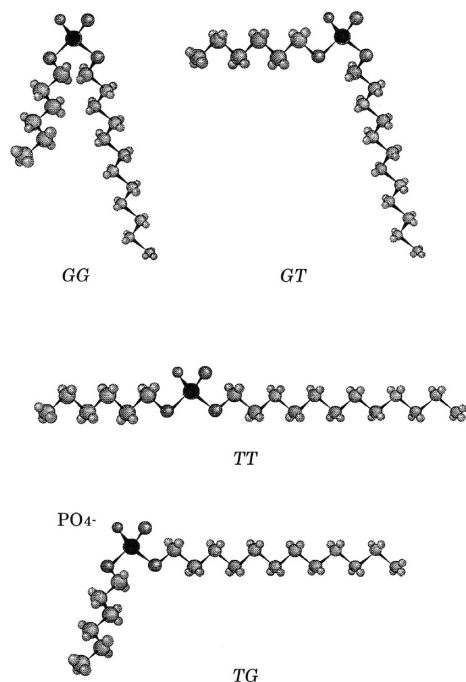
X-ray crystallographic analysis has already been carried out on barium diethyl phosphate (DEP).[13] The two C−O bonds of

Scheme 1. Schematic Representation of the Four Rotational Isomers (GG, GT, TG, and TT) about the P−O Bonds of HDoP[a]

GG   *GT*

TT

PO4-

TG

[a]The conformations about every CH_2–CH_2 bond and the two CH_2–O bonds were assumed to be in the trans (*T*) conformation.

the DEP molecule were found to occupy the gauche (G) positions with regard to the P−O bonds.

Following Raman spectroscopy, normal coordinate analyses of the rotational isomers of the DAP anions[14] were made, indicating that symmetric and antisymmetric O−P−O stretching modes were sensitive to the conformations about the P−O bonds.

Aggregate studies of symmetric and asymmetric DAP anions have been made, using small-angle neutron scattering (SANS).[15,16] Electron microscope images of the microstructure formed by symmetric or long-chain asymmetric DAP molecules have been previously obtained by negative staining TEM[17] and freeze fracture-TEM.[18] The DAP anions with long alkyl chains were found to form vesicles, despite large asymmetries in their chain length.[19]

In the present study, SANS, cryo-TEM, Raman scattering, ^{13}C NMR, and selective NOE ([1]H{[1]H})[20] techniques were used to elucidate the overall structures of aggregates formed by asymmetric DAP anions in aqueous solution. The cryo-TEM observations provided direct images corresponding to the average models predicted by the SANS analyses and the relationship between the microstructures and the conformations, obtained by using these spectroscopic techniques, have been discussed successfully.

■ EXPERIMENTAL SECTION

Materials. Lithium salts of di-*n*-alkylphosphates (DAP) (di-*n*-alkyl: *n*-butyl(*n*-dodecyl)(BDoP) and *n*-hexyl(*n*-dodecyl)-(HDoP)) were synthesized as described previously.[21] Unreacted *n*-alkyl alcohols were extracted exhaustively from the solid surfactants packed into a filter paper thimble, using a Soxhlet extractor (solvent, benzene). Product identification was

made by ^{1}H and ^{13}C NMR spectra and elemental analysis (C, H, and P).

The sample solutions were prepared by weighing DAP and H_2O into glass ampules that were then sealed, and the contents were homogenized by shaking. The phase features of the samples were inspected visually as they were held in a temperature-controlled water bath (284−353 K, rate of temperature elevation and cooling, 0.1 K/min). The cycle of temperature-elevation and cooling with shaking of the samples at the beginning of each cycle was repeated ca. ten times.

Homogeneous and transparent one-phase solutions (region I) were identified at 298 K for BDoP below 0.8 mol/L and for HDoP below 1.0 mol/L. The same intact sample-filled ampules that had been used for visual inspection were allowed to stand at ca. 298 K for ca. one week before measurement of the Raman spectra. Samples used for measurement of SANS, ^{13}C, and ^{1}H NMR spectra were pretreated similarly. These sample solutions were regarded as having attained equilibrium. The C wt % of the samples was transformed to C mol/L using density data.

Cmc Measurements. Equilibrium surface tension (γ_{eq}, mNm^{-1}), electrical conductivity (κ, μS/cm), and ^{13}C NMR chemical shift (δ, ppm) methods were used to obtain the cmc. A Kruss K10 du Nouy surface-tensiometer (platinum−iridium ring: circumference 119.95 mm and radius 9.545 mm) was used to measure the γ_{eq} value. Temperature was controlled at 298 ± 0.1 K by a Grant LTD6G circulator bath. The DAP−H_2O solutions (C mol/L) were prepared using Milli-Q reverse-osmosis purified water. Errors of measured γ_{eq} were ±0.1 mN m^{-1}. Electrical conductivity (κ) was measured with a TOA Conductivity Meter CG-2A and a conductivity cell CG-7001PL (cell constant: 0.995 × 0.1) at 298 ± 0.01 K. ^{13}C NMR chemical shifts method was also used to obtain a second cmc (described separately).

SANS Measurements and Analyses. SANS spectra were measured at 298 ± 0.1 K by use of small- and medium-angle neutron scattering instruments installed at the pulsed neutron source KENS (the National Laboratory for High Energy Physics, Tsukuba, Japan). The DAP sample in D_2O, which was allowed to stand for 7 days at 298 K after preparation, was placed in a quartz cell (path length: 1−2 mm).

The scattering length density (ρ) of each component was calculated using the equation

$$\rho = \sum b_i / V \tag{1}$$

where b_i is the scattering length of atom i, and V is the molecular volume. Literature[22] values of $\sum b_i$ and V were used. The magnitude of the momentum transfer Q is given by

$$Q = (4\pi/\lambda) \sin(\theta/2) \tag{2}$$

where λ is the incident wavelength (3−11 Å for SAN and 1−16 Å for WINK), and θ is the scattering angle. The intensity of the scattered neutrons was recorded on a position-sensitive 2D detector. Normalization of the data to an absolute intensity scale was made by using the transmission of a 1 mm water sample. Corrections for the attenuation of the neutron beam due to absorption and for multiple scattering were also made. The scattering intensity coming from the sample solutions was corrected for the detector background and incoherent scattering. The intensity spectrum of the sample measured below the cmc was subtracted from that of the surfactant solution.

The dependence of the neutron-scattering intensity $d\Sigma(Q)/dQ$ on the magnitude of a scattering vector (Q) can be expressed as a function of both the micellar particle structure factor $P(Q)$ and the interparticle structure factor $S'(Q)$, as follows:

$$d\Sigma(Q)/d\Omega = I_0 P(Q) S'(Q) \qquad (3)$$

where I_0 (cm^{-1}) is the extrapolated zero-angle scattering intensity.

The observed SANS intensity data were analyzed according to the literature.[23−26] A charged micelle model containing a hydrophobic core with a major axis, a, and minor axis, b was applied to calculate $P(Q)$. In this model, the Stern layer of thickness t consists of the head groups, associated with lithium counterions and water molecules, and the hydrated CH_2 groups. $S'(Q)$ for a one-component macro-fluid was calculated using Hayter and Penfold's[25] and Kotlarchyk and Chen's[26] treatments.

The observed scattering intensity data were analyzed with the aggregation number (n), degree of ionization (α) of a macro-ion, and the number of hydrated CH_2 groups (n_{wet}) as fitting parameters, and the values of t, a, and b were calculated using n_{wet} and n.

Cryo-TEM. Cryo-TEM images were obtained to provide direct information on the microstructures of the aggregates. The aqueous solutions of DAP were cooled ultrarapidly, under reduced vapor pressure, to obtain a vitrified quasi-solid state. This process was carried out in a controlled environment vitrification system (CEVS).[27] The specimen thus vitrified was then stored under liquid nitrogen (77 K), until being viewed under the microscope. The specimen was transferred into a Philips CM120 microscope, operated at 120 kV, in an Oxford CT-3500 cooling holder. After equilibration in the microscope at about 93 K, the specimen was examined in the low-dose imaging mode to minimize electron-beam radiation damage. The images were taken at a nominal under-focus of 4−7 nm, where any amplitude contrast is enhanced with phase contrast, and were recorded digitally by a Gatan 791 Multi-Scan CCD camera.

The DAP samples were allowed to stand for 5−6 days at 298 K after preparation, to ensure equilibrium.

Raman Scattering Measurements. The Raman spectra of the solid and aqueous DAP samples were recorded on a Nicolet 950 FT Raman spectrometer at 298 K, using a Nd:YAG laser (CVI) (excitation wavelength: 1064 nm).

^{13}C NMR Measurements. The ^{13}C NMR spectra of the DAP−D_2O samples (isotopic purity of D_2O: 99.9%) (filled in a 10 mm Φ sample tube) were recorded on a Bruker Avance-600 spectrometer, operating at 150.0 MHz (spectral width 238.3496 ppm, 65 536 points in the time domain, acquisition time 0.9110004 s, and delay 6.00 μs) and locked on deuterium, at 298 ± 0.1 K. The observed ^{13}C chemical shifts (δ_{obs}, ppm) (accuracy: ± 0.0001) are given relative to the external standard (1 M $(CH_3)_3Si-(CH_2)_3Na/D_2O$).

^{1}H NMR and Selective ^{1}H{^{1}H} NOE Measurements. ^{1}H NMR spectra of the DAP−D_2O samples (filled in a 5 mm Φ sample tube) were recorded on a Varian XL-300 spectrometer, operating at 300.112 MHz (spectral width, 4500.5 Hz; time domain, 32768 points; acquisition time, 3.641 s; and delay time, 4.000 s) at 298 ± 0.1 K. The ^{1}H chemical shifts (δ, ppm) were measured relative to tetramethylsilane as an external reference. Selective NOE (^{1}H{^{1}H}) difference spectra were measured using the pulse sequence available on the XL-300. Irradiated

power was 8 db, and 16 transients were accumulated for 128 values of evolution period.

RESULTS AND DISCUSSION

Cmcs of the DAP−H_2O Systems. Equilibrium surface-tensions (γ_{eq}) of the sample solutions were measured as a function of C (mol/L) at 298 K. Points of inflection were found in the plots of γ_{eq} against ln C. The concentration corresponding to the inflection point was regarded as the first cmc: 1.87×10^{-3} mol/L for BDoP and 6.0×10^{-4} mol/L for HDoP. The observed values of γ_{eq} followed a quadratic expression below the cmc and were constant above this concentration (Figures not shown). A minimum was not observed in the plots, confirming the high purity of DAP.

Cmc values were also obtained from plots of specific electrical conductivity, κ, against C. In the $\kappa-C$ plots, two inflection points were found for each sample. The concentrations corresponding to the two inflection points at lower and higher concentrations were regarded as the first and second cmc, respectively: for BDoP, 2.64×10^{-3} and 0.06 mol/L; for HDoP, 1.2×10^{-3} mol/L and 0.04 mol/L. The degree of ionization (α_{av}) of the micelles, calculated from the slopes of the two straight lines below and above the first cmc, was 0.60 for BDoP and 0.70 for HDoP. The free energy values (ΔG^0) of micellization per monomer, calculated by use of the equation $\Delta G^0 \approx RT(2 - \alpha_{av}) \ln X_{cmc}$,[28] were −34.5 kJ/mol for both BDoP and HDoP.

The cmc values obtained by surface tension and conductivity methods definitely differ by up to a factor of ca. 2. This difference may be due to the effect of a short (n-butyl or n-hexyl) chain, probably requiring further work for its explanation. The second cmcs corresponded well with those (0.069 mol/L for BDoP and 0.037 mol/L for HDoP) obtained by the ^{13}C NMR chemical shift method (described below).

SANS Spectra and Averaged Microstructures. The SANS spectra of the DAP samples were measured to determine the average aggregation number and the average size and shape of the aggregates. The observed SANS spectra were analyzed for both prolate- and oblate-spheroidal models,[24] assuming monodispersion. The prolate-spheroidal model consistently provided a better fit to the observed SANS intensity data than did the oblate model.

Figure 1 shows the SANS spectra (open circles) of the DAP micelle solutions at various concentrations. Very broad peaks are seen in the curves of $I(Q)$ against Q, indicating the presence of intermicellar interactions in these systems. The interaction peaks increased steadily in intensity and shifted to higher Q values with increasing concentration. This behavior indicates that interactions among micelle particles were enhanced with increasing micelle-concentration.

The calculated scattering intensity profiles (solid lines), providing the best fit between the observed and calculated data, are also shown in Figure 1. The extracted values of n, α, and n_{wet} and the calculated values of t, a, b and $(a + t)/(b + t)$ are listed in Table 1.

Figure 2 shows the n value as a function of the square root of the monomer concentration (molar fraction) $((X - X_{cmc})^{1/2})$ attributable to formation of the micelles (X_{cmc}: molar fraction at cmc).

The plot for BDoP indicates that the average aggregation number n increases linearly with increasing micelle concentration in the range 0.016−0.096 mol/L. A marked change of n was not found at the second cmc (0.06 mol/L).
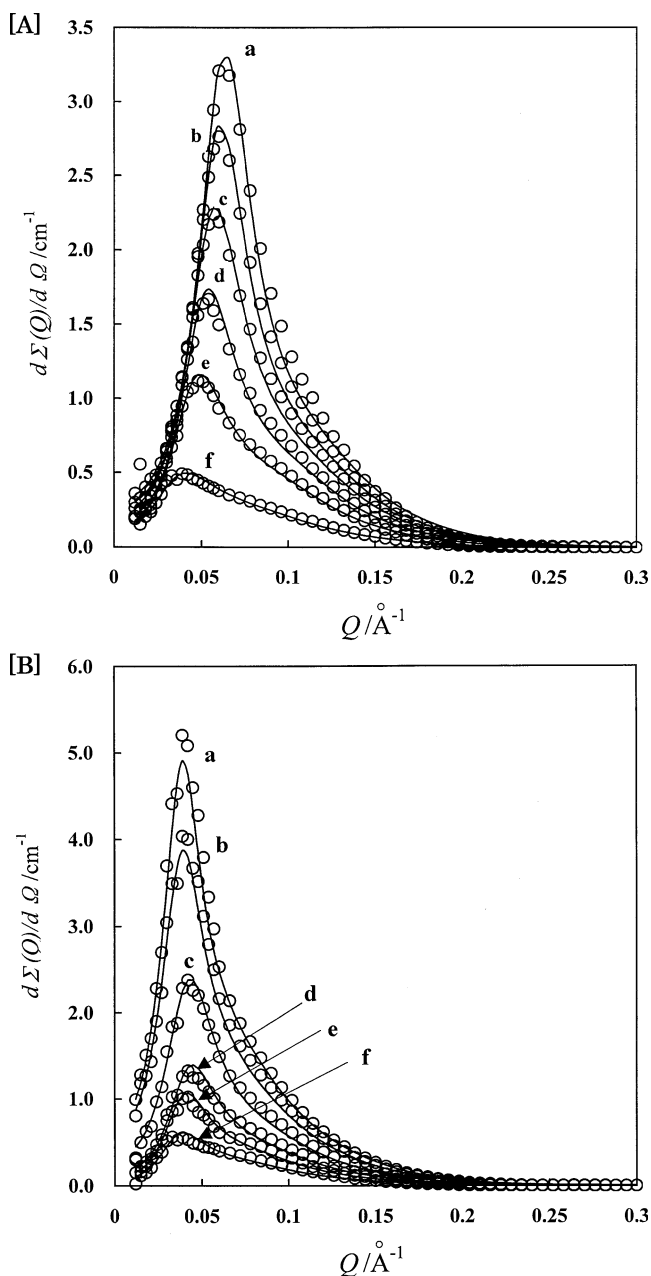
Figure 1. Observed SANS intensity spectra (O) for the DAP-D_2O systems (BDoP [A] a, 0.096 mol/L; b, 0.080 mol/L; c, 0.064 mol/L; d, 0.048 mol/L; e, 0.031 mol/L; f, 0.016 mol/L. HDoP [B] a, 0.074 mol/L; b, 0.060 mol/L; c, 0.045 mol/L; d, 0.030 mol/L; e, 0.022 mol/L; f, 0.014 mol/L) and best-fitted scattering intensity profiles (solid lines).

The plot for HDoP provided two straight lines crossing at a concentration (0.039 mol/L) very close to the second cmc. The higher slope obtained above this point indicates that micelle growth increases markedly above this concentration.

Extrapolation of the straight line in the plots to $X = X_{cmc}$ provides the aggregation number n_0 of a minimum micelle at the first cmc. The values of n_0 were 51.2 for BDoP and 26.5 for HDoP, indicating that micelles of BDoP are larger. The axis ratios $(a + t)/(b + t)$ of the minimum micelles were 1.2 for BDoP and 1.0 for HDoP, supporting a spherical shape for these minimum micelles.

We may apply the Ladder model[29] to explain the growth processes of the micelle systems for BDoP (in the region 0.016−0.096 mol/L containing the second cmc) and for HDoP (in the region 0.014−0.030 mol/L below the second cmc).

The growth of a micelle may be assumed to follow the process now described. At the cmc, the surfactant molecules form a minimum micelle containing n_0 monomers in aqueous solution, and formation of micelles with an aggregation number less than n_0 does not occur. When micelles with $n > n_0$ are formed, the micelle takes a prolate spherocylindrical shape, and n_0 and $n − n_0$ molecules are used for formation of the hemispherical end portions and of the cylinder portion, respectively. According to this model, the formation and growth of the micelles are characterized by the aggregation number (n_0) of a minimum micelle, the free energy change (Δg) per monomer when a surfactant molecule is inserted into the cylindrical portion of a spherocylindrical micelle, and the free energy change (ΔG^0) when n_0 molecules aggregate to form the minimum micelle. The mean aggregation number (n) of a spherocylindrical micelle can be approximated by the equations

$$n = n_0 + 2K^{1/2}(X - X_{cmc})^{1/2} \qquad (4)$$

$$K = \exp(\Delta G^0 - n_0\Delta g)/RT \qquad (5)$$

where X and X_{cmc} are the total concentration and cmc expressed by the molar fraction, respectively. The magnitude of $(\Delta G^0 - n_0\Delta g)$ calculated from the slope $2K^{1/2}$ represents the difference in free energy between n_0 monomers in the two end-caps and the same number of monomeric surfactants in the cylindrical portion.

The ΔG^0 value, obtained from the conductivity measurements, and the slope $2K^{1/2}$ in the plots of n against $(X - X_{cmc})^{1/2}$ were used to calculate the Δg value. The calculated Δg values of BDoP and HDoP were −1.26 and −2.66 kJ/mol, respectively.

The energy differences $(\Delta G^0 - n_0\Delta g)$ of BDoP and HDoP, thus calculated, were 30.05 and 36.27 kJ/mol, respectively. The value of $-(\Delta G^0 - n_0\Delta g)$ provides a measure of the rate of micellar growth as the concentration increases. An increase in short chain-length was found to cause a decrease in the parameter $-(\Delta G^0 - n_0\Delta g)$, indicating that micelles of HDoP grow more rapidly than do those of BDoP.

The axis ratio of BDoP increased linearly with increasing micelle-concentration and did not change rapidly below and above the second cmc (Table 1), indicating that the variation in shape of BDoP micelles proceeded monotonously in this concentration region. For HDoP, a rapid increase of the axis ratio was found above the second cmc (Table 1), showing that a prolate spheroid transforms rapidly to an elongated structure.

The number (n_{wet}) of hydrated CH_2 groups of the dodecyl chain, speculated by the SANS analyses, was ca. 4 − 5 for BDoP and ca. 6 for HDoP (Table 1), implying possible hydration of the butyl or hexyl chains in these micelles. Thus, we may theorize that bulk water molecules may be deeply embedded into the grooves formed by the short chains in these micelles.

From the SANS analyses (Table 1), we may estimate the number (N_s) of water molecules of hydration per one molecule in the micelles. For BDoP, N_s was approximately constant in the concentration region under investigation. However, for HDoP, it decreased rapidly above the second cmc, suggesting a rapid increase in hydrophobicity of the environment around the short chains above this concentration.

Table 1. Extracted Parameters from SANS Analyses of the BDoP [A] and HDoP [B] Micellar Systems[a]

C (mol/L)	n	α	n_{cw}	a (Å)	b (Å)	t (Å)	(a + t)/(b + t)	N_s
[A]								
0.016	61.8	0.25	3.8	26.4	11.9	8.9	1.7	17.2
0.031	65.4	0.31	4.0	27.6	11.7	9.2	1.8	16.6
0.048	68.5	0.32	4.4	30.1	11.2	9.7	1.9	17.7
0.064	71.8	0.30	4.5	31.9	11.0	9.8	2.0	17.7
0.080	75.0	0.31	4.8	34.4	10.6	10.2	2.1	18.5
0.096	77.9	0.30	4.9	36.1	10.5	10.3	2.2	18.6
[B]								
0.014	59.7	0.34	5.7	32.3	9.5	11.3	2.1	25.0
0.022	71.9	0.31	6.0	37.9	9.1	11.7	2.4	22.5
0.030	74.8	0.27	6.0	39.4	9.1	11.7	2.5	22.1
0.045	109.2	0.17	6.2	59.0	8.9	12.0	3.4	20.1
0.060	176.8	0.12	6.0	93.2	9.12	11.7	5.0	16.6
0.074	220.3	0.13	6.3	120.2	8.74	12.1	6.4	17.2

[a] n, the average aggregation number; α, the degree of ionization of a micelle; a and b, the major and minor axes of a prolate micelle; t, the thickness of the Stern layer; N_s, the number of hydrating water molecules per molecule of surfactant in the micelle.
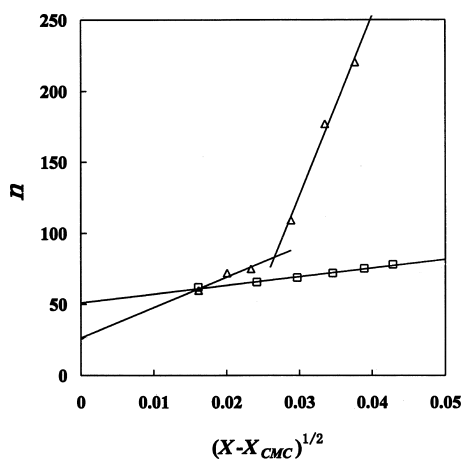

Figure 2. Plot of n as a function of $(X - X_{cmc})^{1/2}$ in the DAP−D$_2$O systems (BDoP (□) and HDoP (Δ)).

Figure 3. Cryo-TEM images of spheroidal micelles for the BDoP sample (0.096 mol/L).

Thus, SANS analyses predict that a difference in the shorter chain-length brings about a marked difference in the aggregational behavior of BDoP and HDoP.

Cryo-TEM Direct Images. The cryo-TEM observations were carried out at the same concentrations as the SANS measurements to obtain direct images of the aggregates.

For the BDoP samples, cryo-TEM images showed that the aggregates were approximately spheroidal in the concentration range 0.016−0.096 mol/L, which included the second cmc (0.06 mol/L) (Figure 3). This result corresponds well to that of the SANS analyses. The SANS analyses also predicted that spheroidal micelles increased in size in this concentration region and their shape changed monotonously (Table 1). However, we were unable to confirm these predictions using the direct imaging process as changes in size were too small to be observed.

In the cryo-TEM images of the HDoP samples, spheroidal micelles were predominant in the concentration region below 0.030 mol/L. The image of the 0.014 mol/L sample as representative is shown in Figure 4A. The images of spheroidal micelles of these samples were similar to those for BDoP (Figure 3). In the image of the 0.045 mol/L sample (Figure 4B), flexible thread-like micelles appeared among the predominant spheroidal micelles. The microstructures of this
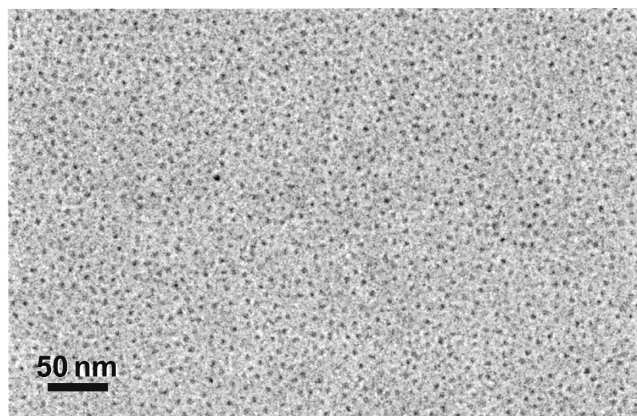
sample were definitely different from those seen at lower concentrations. This result verifies the existence of a second cmc for HDoP. The imaged thread-like micelles correspond to the elongated spheroidal micelles predicted by the SANS analyses.

For the more concentrated samples, 0.074 and 0.098 mol/L, the flexible thread-like micelles became dominant although spheroidal micelles were still visible (a representative image of the latter sample at 0.098 mol/L is shown in Figure 4C). As the concentration of HDoP increased, the proportion of thread-like micelles increased further. Similar observations have been made by Bernheim-Groswasser and co-workers[30a] in the micelles of gemini surfactants. In the images of the 0.098 mol/L sample, uni- and multilamellar vesicles and stiff ribbon-like aggregates were also seen (images not shown).[30b] In particular, the appearance of the long stiff ribbon-like aggregates indicates that a further transition of the thread-like micelles to such aggregates with lower curvatures possibly occurs in higher concentrated samples (to be published separately).

The rapid increase of average aggregation number and axis ratio above the second cmc, predicted by the SANS analyses (Table 1) is due to the increased concentration of flexible thread-like micelles. The cryo-TEM images of the 0.074 and 0.098 mol/L samples give direct evidence that the predicted values of n and the axis ratio are averaged among those of the
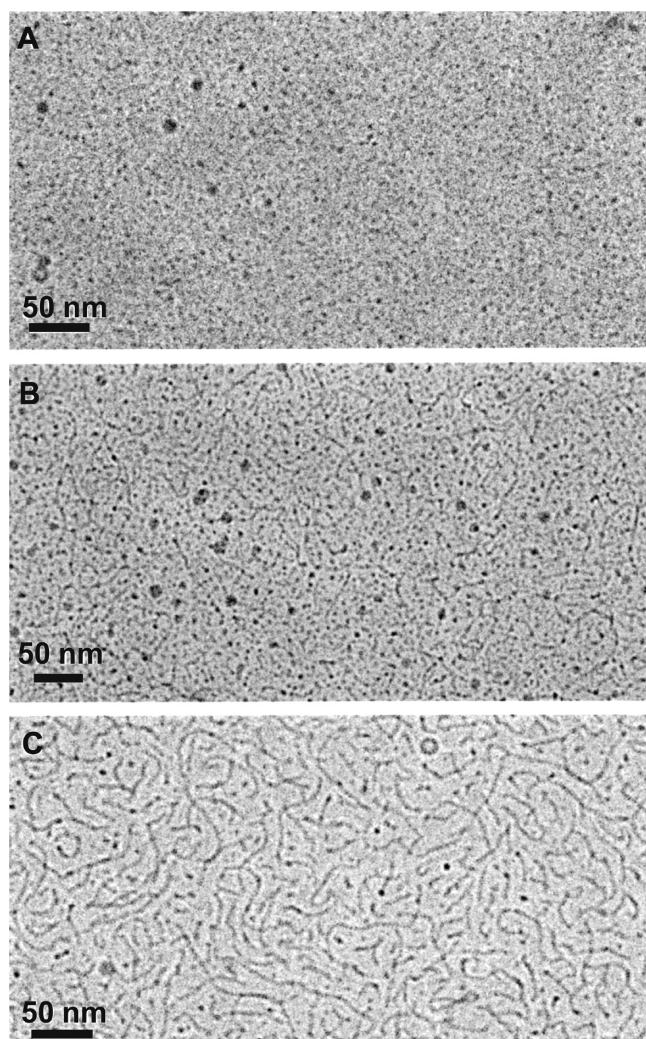
Figure 4. Cryo-TEM images of the HDoP samples: (A) spheroidal micelles at 0.014 mol/L; (B) spheroidal and thread-like micelles at 0.045 mol/L; (C) thread-like micelles at 0.098 mol/L.

dominant thread-like micelles and the few coexisting spheroidal micelles.

The dark spots (Figure 4C) seem to be at the ends of short thread-like micelles but may also be points of a bend, where the micelles become aligned with the electron beam, as pointed out by Vinson and Talmon.[31]

Thus, there exists a marked difference in the concentration-dependence of the cryo-TEM images of BDoP and HDoP, caused by the difference in the short chain length. In particular, the steric effect of a butyl segment may cause formation of nonspherical micelles (described below).

In the cryo-TEM images of BDoP and HDoP, a few round membrane patches with lower curvature structures were seen (Figures 4A,B). These structures are nonequilibrium structures that appear only sporadically. Therefore, they had little influence on the average micelle size and shape predicted by SANS.

The images of BDoP and HDoP seem to be insufficiently resolved, probably due to the sample properties coming from these asymmetric molecular structures.

Raman Scattering Spectra. Analysis of the Raman bands of the solid and aqueous samples was focused on the ν_a(O−P−O) and ν_s(O−P−O) modes in the region 750−850 cm^{-1}

(Table 2), which are sensitive to the conformations about the phosphodiester P−O bonds.[9,14a] The observed Raman bands

Table 2. Observed Raman Band Frequencies (cm^{-1}) and Their Assignment in the Region 700−850 cm^{-1} for BDoP and HDoP in the Solid State and in Aqueous Solution^a

observed^b (cm^{-1})					
BDoP		HDoP			
solid	aq. soln.^{d}	solid	aq. soln.^{d}	assignment^{c,e}	
835$_s$	837$_s$			GG	ν_a(OPO)
821$_m$	820$_m$	823$_s$	823$_{bs}$	GT	ν_a(OPO)
	(810−812)$_{vw}$		(810−814)$_{vw,sh}$	TT	ν_a(OPO)
793$_m$	789$_m$	795$_{sh}$	790$_{bm}$	GG, GT, TG, TT	ν_s(OPO) + r(CH$_2$)

^{a}The ν_a(O−P−O) and ν_s(O−P−O) denote anti-symmetric and symmetric stretching modes of the O−P−O segment, respectively. ^{b}s, strong; m, medium; w, weak; b, broad; sh, shoulder; vw, very weak. $^c\nu_a$ and ν_s, asymmetric and symmetric stretching modes, respectively; r, rocking mode. ^{d}Observed in common for concentrated samples (region II) (1.43 mol/L for BDoP (hexagonal phase); 0.65 mol/L for HDoP (lamellar phase). Bands in parentheses were observed at lower concentrations of region I (isotropic phase) (0.032 and 0.064 mol/L for BDoP and 0.030 and 0.045 mol/L for HDoP). ^{e}Assignment made from the normal-mode analyses in our previous work.[14b,c] Calculated frequencies (cm^{-1}) of the ν_a(OPO) modes for butyl(hexyl)-phosphate[14b] (**bold**) and butyl(dodecyl)phosphate[14c] (in parentheses) are: **831**(838) for GG, **825**(823) for GT, **826**(825) for TG, and **817**(816) for TT.

were assigned on the basis of our previous studies[14b] and the normal-mode analysis of a butyl(cetyl)phosphate anion.[14c]

Conformational Preference about the P−O Bonds. For the BDoP spheroidal-micelle samples (region I), the Raman spectra revealed weak and broad Raman bands at 810−815, 820−823, 825−827, and 835 cm^{-1}, at a concentration of 0.032 mol/L (Figure 5A, part a), assigned to TT, GT, TG, and GG, respectively. Since the micelle molar fraction $(C − \text{cmc})/C$ of this sample is 0.94, the contribution of monomers to these Raman bands must be very small. This observation shows that the four molecular forms may coexist in the spheroidal micelles and that the extent of restriction of the P−O bonds is relatively small in solutions of smaller concentrations of these micelles.

The 835 cm^{-1} band was further intensified in the spheroidal micelle region (0.064−0.096 mol/L) above the second cmc (Figure 5A, parts b and c), indicating further preference for GG during growth of the spheroidal micelles. The intensity of the 820−823 cm^{-1} band also increased in this spheroidal micelle region, indicating that GT is also stabilized.

For the samples at higher concentration (region I: 0.128 and 0.192 mol/L), the 835 cm^{-1} band was further intensified, indicating more preference for GG, although the 820−823 cm^{-1} band also increased in intensity (Figure 5A, parts d and e). Finally, the spectral features became very similar to those of the concentrated BDoP samples (Table 2).

We have also examined the phase structures of the concentrated BDoP samples (region II: 0.8−1.5 mol/L) by use of ^{31}P NMR spectra and X-ray diffraction patterns (to be reported separately). Of special relevance to this present study is confirmation of the existence of hexagonal structures (spacing d(Å): 40.36, 24.77, and 19.55 for 1.43 mol/L).
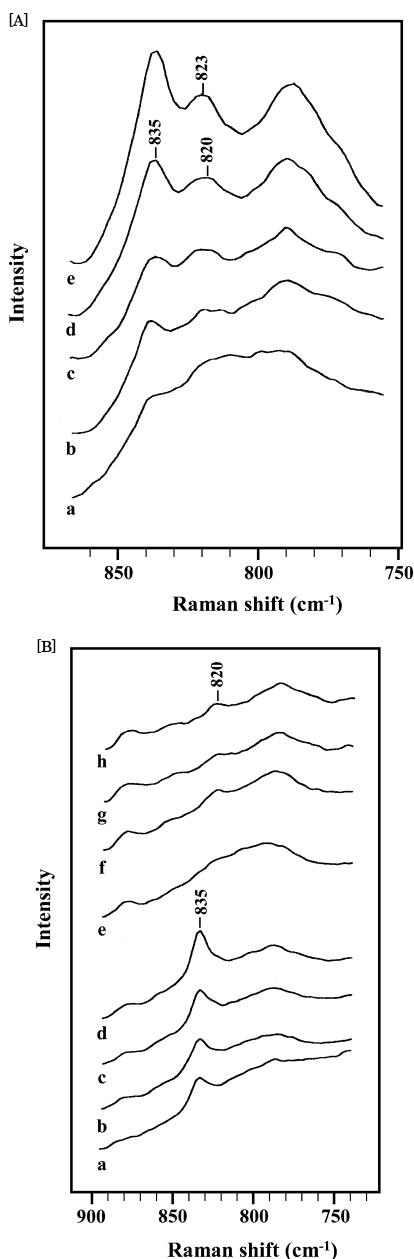
Figure 5. Raman spectra of the DAP−H₂O systems in the 750−850 cm⁻¹ region (BDoP [A] a, 0.032 mol/L; b, 0.064 mol/L; c, 0.096 mol/L; d, 0.128 mol/L; e, 0.192 mol/L. HDoP[B] a, 0.030 mol/L; b, 0.045 mol/L; c, 0.060 mol/L; d, 0.074 mol/L; e, 0.081 mol/L; f, 0.090 mol/L; g, 0.105 mol/L; h, 0.120 mol/L).

The Raman results indicate that, as the concentration of the spheroids increases, the extent of the P−O restriction becomes very similar to that in the hexagonal structure.

The Raman spectra of HDoP in aqueous solution were found to depend strongly on the concentration, as shown in Figure 5B. A very strong band at 835 cm⁻¹ was observed together with very weak and broad bands at 810 and 820 cm⁻¹ for the 0.03 mol/L sample (micelle molar fraction: 0.95) in the spheroidal micelle region (Figure 5B, part a). (Unfortunately, we could not measure the Raman spectra of further diluted samples.) However, this observation shows that the specific molecular form GG was predominantly stabilized and that the fractions of other molecular forms (TT and GT) were very small. Therefore, we may assume that for HDoP, the rotational

freedom about the P−O bonds becomes restricted in the spheroidal micelles, in contrast to BDoP. (The difference in the extent of P−O restriction between BDoP and HDoP reflects the difference in microstructures of their spheroids.)

The 835 cm⁻¹ band was further intensified in the 0.045−0.074 mol/L region above the second cmc (Figure 5B, parts b−d). On the basis of the cryo-TEM data in this region, as the concentration increased, the concentration of thread-like micelles increased, while that of spheroidal micelles decreased. Therefore, the 835 cm⁻¹ band may be regarded as a band characteristic of both flexible thread-like and spheroidal micelles.

We note the marked change in the Raman spectrum of the sample at 0.081 mol/L (Figure 5B, part e). Now, a shoulder band at 835 cm⁻¹ and a weak band at 820−823 cm⁻¹ are observed. A further increase in concentration brought about increased intensity of this 820−823 cm⁻¹ band and decreased intensity of the 835 cm⁻¹ shoulder band (Figure 5B, parts f and g). Since predominant thread-like micelles were imaged in the cryo-TEM of the 0.098 mol/L sample (Figure 4C), this marked spectral change indicates that the conformational transition from GG to GT occurs at higher concentrations of thread-like micelles and that further restriction of the P−O bonds proceeds at higher concentrations of these micelles.

For the 0.120 mol/L sample (Figure 5B, part h), the Raman band at 820 cm⁻¹ was intensified further, and the intensity of the 835 cm⁻¹ band decreased, and the spectral features now approach those of the concentrated HDoP samples in region II (Table 2).

These Raman results may be regarded as evidence for a further transition from the thread-like micelles to lamellar structures. Indeed, for the concentrated samples of HDoP (region II: 1.0 − 3.0 mol/L), the existence of a lamellar structure was confirmed using X-ray diffraction techniques (spacing d(Å): 31.98, 16.72, and 11.30 for 1.78 mol/L). For the lower concentration samples in region II, for which the X-ray patterns characteristic of a lamellar were not observed, the ³¹P NMR spectral features provided evidence for existence of the lamellar fragments (to be reported separately).

¹³C NMR Spectra. The ¹³C NMR spectra of the BDoP and HDoP anions in D₂O were measured at various concentrations at 298 K, to assess variation in the hydrophobic interactions caused by aggregation.[32] A representative ¹³C NMR spectrum of HDoP is shown in Figure 6. Assignment of the resonance peaks was made according to Lindeman and Adams's rule.[33a,b]

The concentration-dependence of the three-bond coupling constant $^3J_{obs}$ (^{31}P−O−C−^{13}C) was also obtained from the ¹³C NMR spectra. Fractional population (P_t) of the trans form
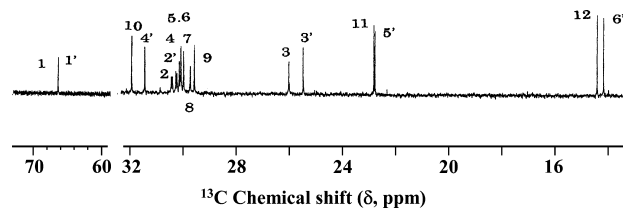

Figure 6. ¹³C NMR spectrum of the HDoP−D₂O solution (0.036 mol/L) and peak assignment (external reference: TMS). The numbering of carbon atoms starts at the polar group side (for the dodecyl chain, the POCH₂ carbon is 1, and the dodecyl CH₃ carbon is 12; for the hexyl chain, the POCH₂ carbon is 1', and the CH₃ carbon is 6').

(T_{POCC}) about the PO—CC single bond was calculated by the use of $^{3}J_{obs}$.[34,35] The values of P_{t} are summarized below.

Below the first cmc of BDoP, the P_{t} values of the *n*-butyl and *n*-dodecyl chains were 0.8 and 0.6, respectively. Above the cmc, they increased up to 0.9 and remained constant at higher concentrations. Below the first cmc of HDoP, the P_{t} value for both *n*-hexyl and *n*-dodecyl chains was 0.6 and increased up to a constant value of 0.9 above the cmc.

These observations indicate that the POCC segments of BDoP and HDoP are extremely restricted in their micellar environment.

^{13}C NMR Chemical Shifts and Hydrophobic Interactions. The observed ^{13}C chemical shift (δ_{obs}, ppm) is a weighted average of the chemical shifts in the monomeric and micellar states since the exchange rate of monomers between the bulk solution and the micelle is generally fast on the NMR time scale. A pseudophase and single-step model has been applied to the isotropic sample solutions in order to explain this change in δ_{obs}.[36a] The δ_{obs} value is expressed by the equation $\delta_{obs} = (cmc/C)\delta_{mono} + [(C - cmc)/C]\delta_{mic}$, assuming that the concentration of monomer is constant above the cmc.[36b] C is the total concentration, and δ_{mono} and δ_{mic} are the ^{13}C chemical shifts in the monomers and micelles, respectively.

For DAP anions in $D_{2}O$, it was found in this present study that the ^{13}C resonance peak of the *n*-dodecyl CH_{3} group shifted low-field with increasing concentration, while that of the *n*-butyl or *n*-hexyl CH_{3} groups shifted high-field (the slopes are listed in Table 3).

Table 3. Concentration-Dependence of Slope (S_{1} and S_{2}, ppm/mol L^{-1}) in the δ_{obs}—C Plots for the Terminal CH_{3} Groups of BDoP and HDoP

BDoP	0.04−0.07 mol/L	above 0.07 mol/L
	S_{1}	S_{2}
dodecyl-CH_{3}	−0.46	−1.51
butyl-CH_{3}	+0.50	+0.30
HDoP	0.01−0.04 mol/L	above 0.04 mol/L
	S_{1}	S_{2}
dodecyl-CH_{3}	−2.90	−0.55
hexyl-CH_{3}	+1.56	+0.72

The shift behavior of the *n*-dodecyl-CH_{3} ^{13}C resonance peak reflects the increased hydrophobic interactions among the *n*-dodecyl chains upon micelle formation. Conversely, for the short chain CH_{3} groups, both a hyper-conjugative interaction of the lone electron pairs of the ether linkage oxygen with the C—C bond of an extended short chain and the effect of counterions binding on the polar head may contribute to the high-field shift.[35] However, it is very difficult to discuss their effects independently.

Therefore, the focus was on the low-field shift of the *n*-dodecyl CH_{3} peak reflecting a change in the hydrophobic interactions, as shown in Figure 7. Inflection points of the straight line plots of δ_{obs} against C, appeared at 0.069 mol/L for BDoP (Figure 7A) and 0.037 mol/L for HDoP (Figure 7B), corresponding well to the second cmcs determined by the conductivity method.

Slopes (ppm/mol L^{-1}) of the two straight lines, which are designated as S_{1} and S_{2} below and above, respectively, the second cmc, are listed in Table 3. S_{1} should reflect the amount of hydrophobic interactions upon micelle formation, and their
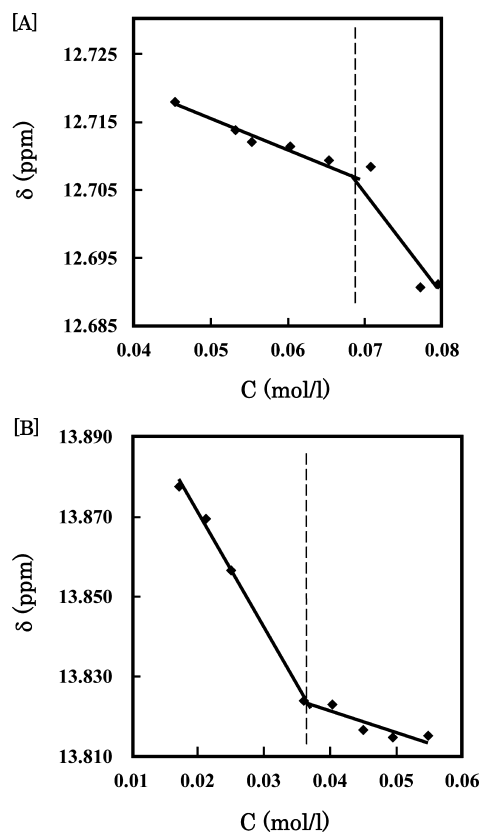

Figure 7. Plots of δ_{obs}−C for the dodecyl CH_{3} groups (BDoP [A] and HDoP [B]).

absolute values may be used as a measure of the extent of increased hydrophobic interactions. The absolute value of S_{1} for BDoP is smaller than that for HDoP, implying that the extent of the increased hydrophobic interactions in formation of spheroidal BDoP micelles is much smaller than that for formation of spheroidal HDoP micelles.

This difference may be ascribed to the difference in proximity among the *n*-dodecyl chains between the two spheroidal micelle systems. Coexistence of four molecular forms about the P—O bonds in spheroidal BDoP micelles (Figure 5A, parts a−c) implies reduced restriction of the polar head, decreasing the hydrophobic interactions among the *n*-dodecyl chains. However, stabilization of a specific isomer GG about the P—O bonds in the growth process results in a gradual increase in proximity among the *n*-dodecyl chains, causing a small slope (S_{1}) in the ^{13}C δ−C plot for BDoP. Conversely, for spheroidal HDoP micelles, preference of the GG form may occur rapidly during growth of the micelles (Raman data, Figure 5B, parts a−d). Such conformational preference leads to a rapid increase in proximity among the *n*-dodecyl chains, bringing about a marked change of S_{1} in the ^{13}C δ−C plot (Figure 7B).

Thus, the difference in S_{1} between BDoP and HDoP reflects the difference in the packing state of the *n*-dodecyl chains in the two spheroidal micelle systems.

The difference in the extent of further ordering of the hydrocarbon chains may contribute to the difference in slopes (S_{2}) above the second cmc. For BDoP, further stabilization of GG (Figure 5A) may increase the extent of hydrophobic interactions, causing a rapid change in the slope. For HDoP, the fact that S_{2} (reflecting the growth of thread-like micelles) is smaller than S_{1} may come from preference for GG in both
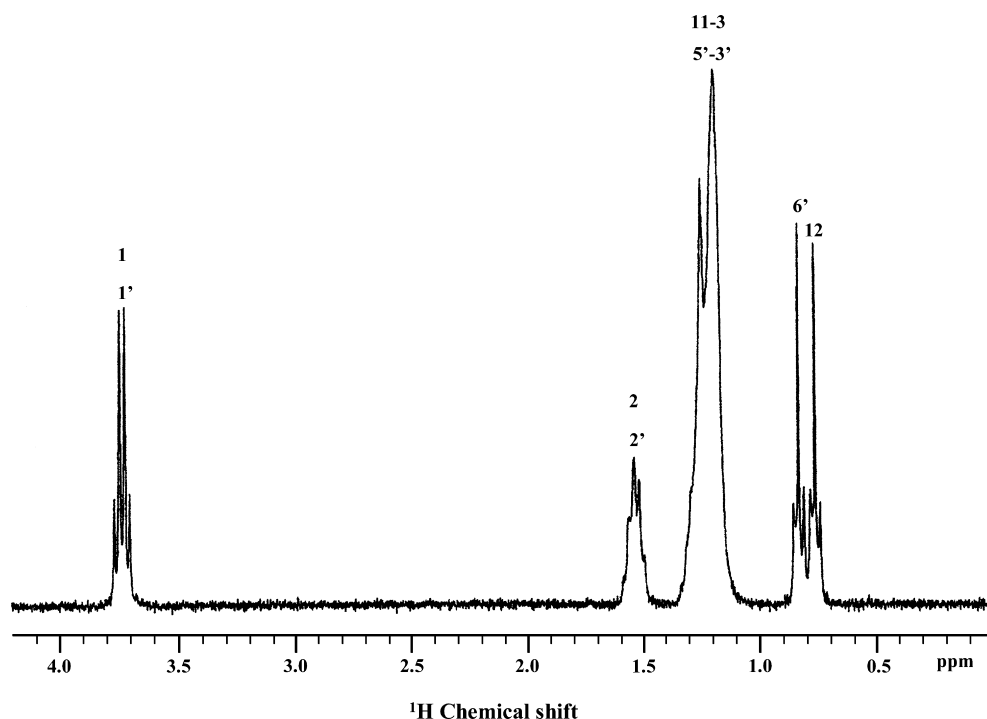
Figure 8. Nonirradiated ^{1}H NMR spectrum of the HDoP−D_2O sample (0.035 mol/L) and peak assignment (the numbering of the resonance peaks corresponds to that in Figure 6).

spheroidal and thread-like micelles, implying a similar directionality of the two hydrocarbon chains in both micelle systems. That is, further ordering of the hydrocarbon chains during the transition from spheroidal to thread-like micelles is less marked, and thus, S_2 is smaller.

Selective NOE and Spatial Proximity of the Two Chains. To confirm further ordering of the hydrocarbon segments below and above the second cmc, ^{1}H{^{1}H}NOE experiments[37] were made for BDoP and HDoP using a selective decoupling method.

Figure 8 shows the nonirradiated ^{1}H NMR spectrum of a representative HDoP−D_2O sample (0.017 mol/L). The ^{1}H resonance peaks were assigned on the basis of ^{1}H NMR spectra of simple asymmetric DAP samples.[33b] The intensities of the 1,1'- and 2,2'-CH_2 signals decreased under low-power decoupling of the short chain CH_3 protons (4' for BDoP and 6' for HDoP), indicating the presence of NOE.[20,37]

The NOE value observed in the 1,1'- or 2,2'-CH_2 signals of each sample relative to that observed in the same signals of the lowest concentration sample (relative NOE value) was calculated for BDoP and HDoP.

Figure 9 shows the concentration-dependence of the relative NOE value for the HDoP samples (using the lowest concentration: 0.017 mol/L) as a representative. The relative NOE value was found to reduce markedly below and above the second cmc. This phenomenon indicates that intra- or intermolecular distances from the 6'-CH_3 protons to the 1,1'- and 2,2'-CH_2 protons increase rapidly above the second cmc. Since the concentration of thread-like micelles increases above the second cmc, this rapid variation may be caused by further ordering of the hydrocarbon chains attended by the transition from spheroidal to thread-like micelles.

For the conformation about the CH_2−CH_2 bond adjacent to the bulky polar group, predominant stabilization of the trans form has been confirmed by the Raman spectra of simple
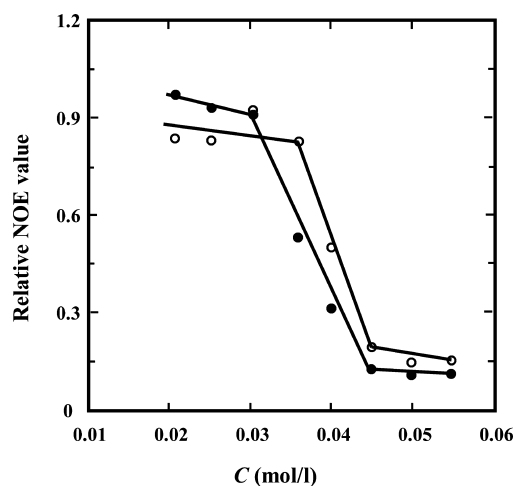

Figure 9. Concentration-dependence of the relative NOE value for the HDoP−D_2O samples at 298 K (●, 1,1'-CH_2 protons; ○, 2,2'-CH_2 protons).

surfactants.[3b] Furthermore, in the present study, it was confirmed from the $^3J_{obs}$ observation that the trans conformation about the PO−CH_2(1,1')CH_2(2,2') segment was stabilized predominantly upon aggregation, implying that this segment is extremely restricted. Therefore, when we consider variation of the distance from the n-hexyl-CH_3 protons to the 1,1'- and 2,2'-CH_2 protons, we may consider the origin to be either the CH_2(1,1') or CH_2(2,2') protons. We may then assume that the conformational change of the n-hexyl chain causes a large change in this distance, resulting in the NOE phenomenon (described below).

Conversely, for BDoP, the relative NOE value decreased linearly and gradually in the 0.035−0.10 mol/L region containing the second cmc (plots not shown). In contrast to

the case for HDoP, a rapid change of the relative NOE value above the second cmc was not found. This fact indicates a monotonous increase in the intra- or intermolecular distance from the 4′-CH$_3$ to the 1,1′- and 2,2′-CH$_2$ groups, reflecting gradual ordering of the *n*-butyl chains during growth of the spheroidal BDoP micelles. The absence of a rapid change in the relative NOE value above the second cmc may be explained by the steric effect of the *n*-butyl segments (described below).

Spheroidal and Thread-Like Micelle Models. A marked difference in the aggregational behavior of BDoP and HDoP may be ascribed to the difference in the extent of the steric effect between the *n*-butyl and *n*-hexyl chains.[38−40] The conformations about the CH$_2$−CH$_2$ single bond, as well as those about the P−O bonds, may be concerned with such a difference in the steric effect. In the present study, the conformations (trans and gauche forms) of a hydrocarbon chain are designated by bold and italicized *T* and *G* to distinguish them from the conformations about the P−O bonds.

In the Raman spectra of liquid paraffin (CH$_3$(CH$_2$)$_n$CH$_3$, *n* = 3),[2c] a strong band due to the *all-trans* (*TT*) form and very weak bands arising from the *TG* form have already been observed, indicating that the extended *TT* chain was stabilized predominantly in the liquid state and that the population of the *TG* form was very small (designated by *TT* ≫ *TG*). Furthermore, for the liquid species of *n* = 4, the population of the conformations increased in the order of *TTT* > *GTT* or *TGT* and for the liquid *n* = 6 species; its order was *TTTT* > *GTTT* > *TGTT*.[2c] The results imply that the small conformational free-energy difference[2b] also stabilized the other forms containing *G* as well as the predominant *all-trans* forms. The order of these conformational stabilities may be applied to simple surfactant systems.

Accordion-like vibrational modes have been measured by the Raman scattering method for aqueous samples of simple soap molecules[3,6] and simple di-*n*-alkylphosphates.[5,12] The results proved directly that the population of an extended hydrocarbon segment increased upon aggregation. These observations are direct evidence that even simple surfactants are able to form aggregates through hydrophobic interactions among the extended short-hydrocarbon segments.

The results of the SANS analyses, cryo-TEM, Raman scattering, and ^{13}C NMR (chemical shifts and $^3J_{obs}$) reported in this study, in addition to the results of simple paraffin and surfactants,[2,3b,4,5,12] were used to estimate the micelle structures.

The conformations of an *n*-butyl segment were confined only to *TT*, *GT*, and *TG* (from the polar side to the terminal CH$_3$). The latter two forms are termed bent-forms. The mirror images *G′T* and *TG′* were regarded as the same molecular forms as *GT* and *TG*. *GG* and *G′G′* were not considered because of their possible instability caused by steric hindrance. Similarly, for an *n*-hexyl segment, only *TTTT*, *TTTG*, and *TTGT* were considered. The last two forms are also termed bent-forms.

In the SANS prediction, the BDoP micelles are spheroid (Figure 10A, part a), and the minimum micelle with the axis ratio 1.2 at the first cmc may be regarded approximately as a sphere. However, this slight deviation (0.2) from the axis ratio 1 of a sphere may become a cause of the growth as a spheroidal micelle. Moreover, the SANS analyses predicted that the n_0 value of a minimum BDoP micelle is twice that of HDoP (Figure 2). This finding may be explained as follows.
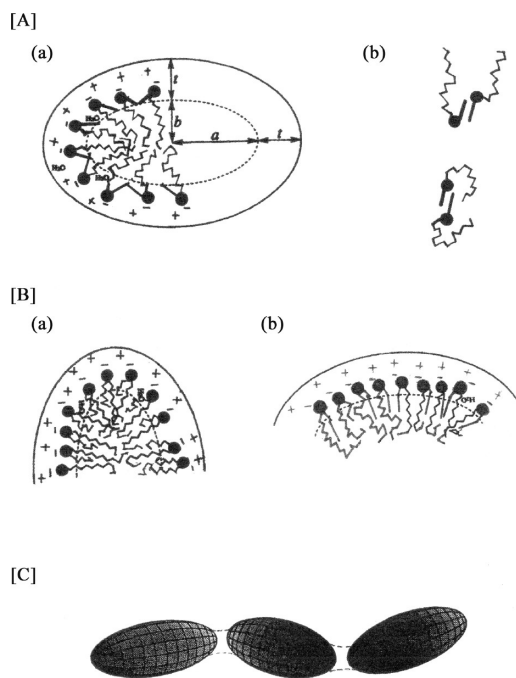

Figure 10. Schematic models: [A] (a) spheroidal BDoP micelle model I; (b) dimer-models; [B] (a) microstructure-model II of a spheroidal HDoP micelle; (b) microstructure-model II′ of a thread-like HDoP micelle; [C] formation-model III of a flexible thread-like micelle.

For BDoP in the monomolecular dispersion state, the probability of taking the *all-trans* (*TT*) must be relatively high. Therefore, dimeric aggregates of BDoP may be first formed by mutual stacking of the two *TT* forms through their hydrophobic interactions (Figure 10A, part b). Further aggregation of the dimers thus formed occurs successively through hydrophobic interactions among the *n*-dodecyl chains, finally providing a minimum micelle of n_0 equal to ca. 52.

Thus, most of the *n*-butyl-oxy segments are already extended in the BDoP aggregates, and the contribution of bent-structures to the micelle structure must be small. In the aggregates, therefore, the extended *n*-butyl segments may prevent close proximity among the *n*-dodecyl segments. In the minimum micelles thus formed, the surfactant molecules may be loosely packed (model I, Figure 10A, part a). Hindering of further proximity among the *n*-dodecyl chains, due to the extended segment effect, may be continued throughout the whole process of growth as a spheroid, causing little change in the micelle shape. Moreover, this *all-trans* chain effect may give rise to many grooves, like fjords, into which bulk water molecules may easily invade in the micellar polar region.

From the SANS analyses, the conclusions for the number of hydrated CH$_2$ groups and for the slow speed of micelle-growth support this loosely-packed model. The P−O restriction behavior, estimated from the Raman spectra, and the S$_1$ behavior of the ^{13}C NMR δ_{obs}, both obtained in the spheroid region, may be also explained by this model.

In micelle formation of HDoP, the *n*-hexyl chain should provide a more hydrophobic environment than the shorter *n*-butyl chain, as suggested in the gemini surfactant systems.[38−40] Therefore, the *n*-hexyl segments of HDoP may favor affinity for the *n*-dodecyl chains through hydrophobic interactions. This effect may be enhanced by preferential stabilization of GG about the P−O bonds. Thereby, as the *n*-dodecyl chains become closer to each other, their hydrophobic interactions

increase, resulting in the formation of a minimum spherical micelle.

In this minimum micelle model, the HDoP molecules may be more closely packed than those of BDoP and the population of bent-forms, in addition to the *all-trans* form, may be relatively high. As the concentration increases, an increase in the population of the *all-trans* form strengthens hydrophobic interactions between the *n*-hexyl and *n*-dodecyl chains, promoting the speed of micelle growth. The steric effect of this *all-trans* chain may be weaker than that of the *n*-butyl chains since the probability of taking the *all-trans* form is undoubtedly small, compared with that for the *n*-butyl chain. However, this effect may stimulate the growth of a spheroidal shape. This growth process may continue until the order of conformational populations finally attains the order *TTTT* > *GTTT* > *TGTT*. Coexisting flexible bent-structures, in addition to the *all-trans* form, may also result in grooves in the polar area and invasion of bulk water. Concurrently, the *n*-dodecyl chains may bend to fill the space formed in the micelle interior by extended- and bent-*n*-hexyl chains (model II, Figure 10B, part a).

This spheroidal model may explain well the Raman scattering and ^{13}C chemical shift results as well as the SANS predictions obtained below the second cmc.

Model of Spheroid to Thread-Like Micelle Transition. In our previous article,[41] the one-dimensional aggregate theory has been applied to the rod-like aggregates of L-glutamic acid oligomers, elucidated by the use of IR, SANS, and SAXS spectra. The results demonstrated that the one-dimensionally stacked rod-like aggregates become unstable with an increase in residue number (N_p) until an aggregate structure may finally be broken at $N_p > 14$. This restriction implies that the shape of an aggregate may be maintained until its size attains the limiting value and that variation of the shape may occur beyond the limit. The concept of this limiting size may be applied to the proposed spheroid to thread-like micelle transition.

We present a model for this transition. When the relative populations of the *all-trans* and bent-structures attain the order *TTTT* > *GTTT* > *TGTT* at the second cmc, the axis ratio of a spheroid micelle has reached the limiting value (that is, limiting size), thus providing a trigger for appearance of a thread-like micelle. Spheroidal micelles, which have attained the limiting axis ratio of ca. 3 (aggregation number: ca. 100), may possibly fuse together cooperatively at the second cmc, leading to the final presentation of flexible elongated structures.

The change from bent to extended conformations, during the process of attainment of conformational stability, brings about a marked increase in an intra- or intermolecular distance from the 1,1′- and 2,2′-CH$_2$ protons to the *n*-hexyl-CH$_3$ protons, resulting in marked variation of the relative NOE value (Figure 9). Thus, the present NOE results may support this transition model.

A more detailed identification of such a dynamic structure during the transition may be lead to elucidation of its mechanism. Use of two-dimensional nuclear Overhauser effect spectroscopy (NOESY) and rotating-frame Overhauser enhancement spectroscopy (ROESY)[20,37] is highly desirable in this sense.

From the ^{13}C chemical shift data, we may assume that, in this thread-like micelle model (model II′, Figure 10B, part b), the space formed by the extended *n*-hexyl chains inside the micelle of HDoP may be filled by half-portions of the CH$_3$ side of the *n*-dodecyl chains, and the terminal CH$_3$ portions may be more densely packed than in BDoP, causing the order S_1(HDoP) > S_1(BDoP) in the δ_{obs}−C plots.

For the AOT−decane−water system, results of pressure-dependent neutron spin echo experiments[42] provided evidence that the hardness of a lamellar induced under high pressure is greater than that of a droplet. Furthermore, it has recently been suggested that the difference in hardness between the lamellar and droplet structures may be attributed to the conformational change of a surfactant molecule from the solvent-inclusion to the solvent-exclusion type.[2a,2d] The Raman scattering and SANS data in the present study support this concept.

The flexibility of a thread-like micelle of HDoP may be associated with such a conformational change since this quality arises from the softness of its membrane structure. Indeed, in a spheroidal micelle, in which the GG form about the P−O bonds is stabilized (Figure 5B, part a), the solvent-rich shell, containing fjord-like grooves imbedded by water molecules of hydration, may surround the hydrophobic core (theorized from the SANS analyses). In the thread-like micelles, preference of the GG form progresses further (Figure 5B, parts b−d), and while a solvent-rich layer still exists, the number of hydrating water molecules tends to decrease with its growth (again theorized from the SANS analyses). Therefore, the GG form may be regarded as a solvent-inclusion type, causing softness of the membrane structure.

The growth model of a flexible thread-like structure may be described as follows (Figure 10C). In the limiting-size spheroid, which consists of two hemispherical caps and a cylindrical portion (the Ladder model),[29] the extent of solvent-inclusion in the two end-caps may be greater than that in the cylinder, causing fusion among the solvent-rich end portions (Figure 10C).

Conversely, the GT form may be due to a solvent-exclusion type for the following reason. The X-ray diffraction patterns of the concentrated HDoP samples (region II) allowed calculation of the thickness of a lamellar, equal to 18.9 Å. This value is much smaller than that (30.8 Å) calculated using Tanford's equation (l_{max} = 1.5 + 1.265n_m, where l_{max} is the maximum length of the hydrocarbon chain, and n_m is the number of CH$_2$ groups in the chain).[43] The difference in the two values may be accounted for by invoking a closely packed model[44] in which the two surfactant molecules combine alternatively with each other to form the lamellar structures. We may now assume that the lamellar structures gave rise to a further decrease in the number of hydrating water molecules (compared with that in the thread-like micelles), causing a greater hardening of the highly organized aggregates.

More detailed studies are needed for elucidation of the transition from thread-like micelles to such low-curvature structures.

■ CONCLUSIONS

The microstructures of isotropic solutions of the asymmetric di-*n*-alkylphosphates, BDoP and HDoP, were investigated by use of the SANS, cryo-TEM, Raman scattering, C^{13} NMR, and ^{1}H{^{1}H}NOE methods.

SANS analyses showed that the average aggregation number and axis ratio of the prolate spheroidal micelles of BDoP increased gradually in the concentration region containing the second cmc and that micelle growth followed the Ladder model. Conversely, for HDoP, a rapid change of the aggregation number and the axis ratio occurred at the second

cmc, and there was a marked change in the average shape and size of the micelle.

From the cryo-TEM direct images, it was shown that, for BDoP, dominant microstructures were spheroidal, corresponding well to the average aggregate shape predicted by SANS.

For HDoP at lower concentrations, the microstructures were also spheroidal micelles, but at concentrations higher than the second cmc, flexible thread-like micelles with lower curvatures were found, corresponding to an average of elongated structures, as predicted by SANS.

The results from Raman scattering, ^{13}C NMR and selective ^{1}H{^{1}H}NOE analyses strongly supported the conclusion that the conformational change of a surfactant molecule is intimately associated with variation of its aggregated structure. Selective NOE was a particularly powerful tool for investigation of the detailed dynamic structure in the transition from spheroidal to thread-like micelles.

The micelle models presented herein are based on these experimental results.

■ AUTHOR INFORMATION

Notes

■ ACKNOWLEDGMENTS

■ REFERENCES

(1) Israelachvili, J. N. *Intermolecular and Surface Forces*, 2nd ed.; Academic Press: New York, 1992.

(2) (a) Ghosh, S.; Ichiyanagi, N.; Okabayashi, H.; Takeda, T.; O'Connor, C. J. *Bull. Chem. Soc. Jpn.* **2009**, *82*, 664−674. (b) Mizushima, S.-I.; Shimanouchi, T. *J. Am. Chem. Soc.* **1949**, *71*, 1320−1324. and references therein. (c) Schaufele, R. F. *J. Chem. Phys.* **1968**, *49*, 4168−4175.

(3) (a) Okabayashi, H.; Okuyama, M.; Kitagawa, T. *Bull. Chem. Soc. Jpn.* **1975**, *48*, 2264−2269. (b) Okabayashi, H.; Okuyama, M.; Kitagawa, T.; Miyazawa, T. *Bull. Chem. Soc. Jpn.* **1974**, *47*, 1075−1077.

(4) Okabayashi, H.; Abe, M. *J. Phys. Chem.* **1980**, *84*, 999−1005.

(5) Okabayashi, H.; Ikeda, T.; Matsuura, H.; Kitagawa, T. *J. Am. Chem. Soc.* **1982**, *104*, 5399−5402.

(6) Tsukamoto, K.; Ohshima, K.; Okabayashi, H.; Matsuura, H. *J. Chem. Soc., Faraday Trans., 1* **1987**, *83*, 789−800.

(7) Okabayashi, H.; Izawa, K.; Sumiya, A.; Eastoe, J.; O'Connor, C. J. *Bull. Chem. Soc. Jpn.* **2010**, *83*, 651−659.

(8) Jayaram, B.; Ravishanker, G.; Beveridge, D. L. *J. Phys. Chem.* **1988**, *92*, 1032−1034.

(9) Shimanouchi, T.; Tsuboi, M.; Kyougoku, Y. *Adv. Chem. Phys.* **1964**, *7*, 435−498.

(10) Garrigou-Lagrange, C.; Bouloussa, O.; Clement, C. *Can. J. Spectrosc.* **1976**, *21*, 75−82.

(11) (a) Gibson, K. D.; Sheraga, H. A. *Proc. Natl. Acad. Sci. U.S.A.* **1967**, *58*, 420−427. (b) Dunfield, L. G.; Burgess, A. W.; Scheraga, H. A. *J. Phys. Chem.* **1978**, *82*, 2609−2616.

(12) Okabayashi, H.; Miyagai, K.; Uehara, T.; Nishio, E. *J. Phys. Chem.* **1991**, *95*, 7932−7938.

(13) Kyougoku, Y.; Iitaka, Y. *Acta Crystallogr.* **1966**, *21*, 49−57.

(14) (a) Brown, E. B.; Brown, K. G.; Person, W. B. *J. Raman Spectrosc.* **1981**, *11*, 356−362. (b) Okabayashi, H.; Hirata, H.; Suzuki, Y.; Mathew, C. *Vib. Spectrosc.* **1996**, *10*, 239−251. (c) Fujita, T. *Phase Diagrams and Phase Structures of Di-n-alkylphosphates in Aqueous Solutions.* Master's Thesis, Nagoya Institute of Technology, 2000.

(15) Hirata, H.; Okabayashi, H.; Furusaka, H.; Kawakatsu, T. *Colloid Polym. Sci.* **1995**, *273*, 1193−1200.

(16) Hirata, H.; Katayama, S.; Okabayashi, H.; Furusaka, M.; Kawakatsu, T. *Colloid Polym. Sci.* **1996**, *274*, 245−252.

(17) Wagenaar, A.; Rupert, L. A. M.; Engberts, B. F. N.; Hoekstra, D. *J. Org. Chem.* **1989**, *54*, 2638−2642.

(18) Smits, E.; Blandamer, M. J.; Briggs, B.; Cullis, P. M.; Engberts, J. B. F. N. *Recl. Trav. Chim. Pays-Bas* **1996**, *115*, 37−43.

(19) Streefland, L.; Wagenaar, A.; Hoekstra, D.; Engberts, J. B. F. N. *Langmuir* **1993**, *9*, 219−222.

(20) Yoshino, A.; Okabayashi, H.; Kushida, K. *J. Phys. Chem.* **1996**, *100*, 9592−9597.

(21) McCombie, H.; Saunders, B. C.; Stacy, G. J. *J. Chem. Soc.* **1945**, 380−382.

(22) Sears, V. F. *Methods of Experimental Physics*; Academic Press: London, U.K., 1986; Vol. 23, Part A, pp 521−550.

(23) Bendedoch, D.; Chen, S. H.; Koehler, W. C. *J. Phys. Chem.* **1983**, *87*, 2621−2628.

(24) Etori, H.; Hirata, H.; Yamada, Y.; Okabayashi, H.; Furusaka, M. *Colloid Polym. Sci.* **1997**, *275*, 263−273.

(25) (a) Hayter, J. B.; Penford, J. *Mol. Phys.* **1981**, *42*, 109−118. (b) Hansen, J. P.; Hayter, J. B. *Mol. Phys.* **1982**, *46*, 651−656.

(26) Kotlarchyk, M.; Chen, S. H. *J. Chem. Phys.* **1983**, *79*, 2461−2469.

(27) Bellare, J. R.; Davis, H. T.; Scriven, L. E.; Talmon, Y. *J. Electron Microsc. Tech.* **1988**, *10*, 87−111.

(28) Berr, S. S. *J. Phys. Chem.* **1987**, *91*, 4760−4765.

(29) Missel, P. J.; Mazer, N. A.; Benedek, G. B.; Young, C. Y.; Carey, M. C. *J. Phys. Chem.* **1980**, *84*, 1044−1057.

(30) (a) Bernheim-Groswasser, A.; Zana, R.; Talmon, Y. *J. Phys. Chem. B* **2000**, *104*, 4005−4009. (b) Weihs, D. *Rheological and Optical Characterization of Complex Fluids.* Master's Thesis, Technion-Israel Institute of Technology, 2000.

(31) Vinson, P. K.; Talmon, Y. *J. Colloid Interface Sci.* **1989**, *133*, 288−289.

(32) Matsushita, K.; Okabayashi, H. *Chem. Scr.* **1980**, *15*, 69−72.

(33) (a) Lindeman, L. P.; Adams, J. Q. *Anal. Chem.* **1971**, *43*, 1245−1252. (b) Hirata, H.; Maegawa, L.; Kawamatsu, T.; Okabayashi, H. *Colloid Polym. Sci.* **1996**, *274*, 654−661.

(34) Yoshino, A.; Sugiyama, N.; Okabayashi, H.; Taga, K.; Yoshida, T.; Kamo, O. *Colloids Surf.* **1992**, *67*, 67−79.

(35) Wehrli, F. W.; Wirthlin, T. *Interpretation of Carbon-13 NMR Spectra*; Heyden: London, U.K., 1976.

(36) (a) Wennerström, H.; Lindman, B.; Söderman, O.; Drakenberg, T.; Rosenholm, J. B. *J. Am. Chem. Soc.* **1979**, *101*, 6860−6864. (b) Jonsson, B.; Lindman, B.; Holmberg, K.; Kronberg, B. *Surfactants and Polymers in Aqueous Solution*; John Wiley & Sons: New York, 1998.

(37) Jeener, J.; Meier, B. H.; Bachmann, P.; Ernst, R. R. *J. Chem. Phys.* **1979**, *71*, 4546−4553.

(38) Alami, E.; Beinert, G.; Marie, P.; Zana, R. *Langmuir* **1993**, *9*, 1465−1467.

(39) Danino, D.; Talmon, Y.; Zana, R. *Langmuir* **1995**, *11*, 1448−1456.

(40) Zana, R.; Talmon, Y. *Nature* **1993**, *362*, 228−229.

(41) Ishida, M.; Takai, M.; Okabayashi, H.; Masuda, H.; Furusaka, M; O'Connor, C. J. *Phys. Chem. Chem. Phys.* **2001**, *3*, 3140−3149.

(42) Seto, H.; Nagao, M.; Kawabata, Y.; Takeda, T. *J. Chem. Phys.* **2001**, *115*, 9496−9502.

(43) Tanford, C. *J. Phys. Chem.* **1972**, *76*, 3020−3024.

(44) Hirata, H.; Maegawa, K.; Kawamatsu, T.; Kaneko, S.; Okabayashi, H. *Colloid Polym. Sci.* **1996**, *274*, 654−661.